# ACS OMEGA

Article

http://pubs.acs.org/journal/acsodf

# All-Oxide Thermoelectric Module with in Situ Formed Non-Rectifying Complex p−p−n Junction and Transverse Thermoelectric Effect

Nikola Kanas,[†,‡] Michael Bittner,[‡] Temesgen Debelo Desissa,[§] Sathya Prakash Singh,[†] Truls Norby,[§] Armin Feldhoff,[‡] Tor Grande,[†] Kjell Wiik,[†] and Mari-Ann Einarsrud*,[†]

[†]Department of Material Science and Engineering, NTNU Norwegian University of Science and Technology, 7491 Trondheim, Norway

[‡]Institute of Physical Chemistry and Electrochemistry, Leibniz University, 30167 Hannover, Germany

[§]Department of Chemistry, Centre for Materials Science and Nanotechnology, University of Oslo, 0315 Oslo, Norway

S Supporting Information

**ABSTRACT:** All-oxide thermoelectric modules for energy harvesting are attractive because of high-temperature stability, low cost, and the potential to use nonscarce and nontoxic elements. Thermoelectric modules are mostly fabricated in the conventional $\pi$-design, associated with the challenge of unstable metallic interconnects at high temperature. Here, we report on a novel approach for fabrication of a thermoelectric module with an in situ formed p−p−n junction made of state-of-the-art oxides $Ca_3Co_{4-x}O_{9+\delta}$ (p-type) and $CaMnO_3$−$CaMn_2O_4$ composite (n-type). The module was fabricated by spark plasma co-sintering of p- and n-type powders partly separated by insulating $LaAlO_3$. Where the n- and p-type materials originally were in contact, a layer of p-type $Ca_3CoMnO_6$ was formed in situ. The hence formed p−p−n junction exhibited Ohmic behavior and a transverse thermoelectric effect, boosting the open-circuit voltage of the module. The performance of the module was characterized at 700−900 °C, with the highest power output of 5.7 mW (around 23 mW/cm$^2$) at 900 °C and a temperature difference of 160 K. The thermoelectric properties of the p- and n-type materials were measured in the temperature range 100−900 °C, where the highest $zT$ of 0.39 and 0.05 were obtained at 700 and 800 °C, respectively, for $Ca_3Co_{4-x}O_{9+\delta}$ and the $CaMnO_3$−$CaMn_2O_4$ composite.

Cross-section of the module
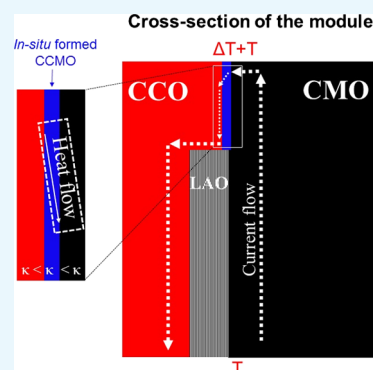
## 1. INTRODUCTION

Energy harvesting from waste heat from, for example, combustion engines or metallurgical processes or other industry has great potential for energy savings and emission reductions. Thermoelectric generators (TEGs) present a promising technology for such energy recovery.[1] A TEG is based on two dissimilar materials (p- and n-types) connected together and when exposed to a temperature gradient, converts thermal energy into electrical energy.[1,2] Power density ($P_{density}$) and the figure of merit ($zT$) are used to evaluate TE modules and their consisting p- and n-type materials, respectively. Figure of merit for any p- or n-type material can be calculate using

$$zT = \frac{S^2 \sigma T}{\kappa} \tag{1}$$

where $S$, $\sigma$, and $\kappa$ represent Seebeck coefficient, electrical conductivity, and thermal conductivity, respectively.[3] In a conventional module ($\pi$-design), p- and n-type materials are connected electrically in series and thermally in parallel, with conductive metallic interconnects between legs (mostly Ag or Au).[4,5] Conventional modules normally suffer from limited temperature, which obstructs the high-temperature advantage

of oxides. Furthermore, conventional modules demonstrate short lifetimes because of the instability of the metallic interconnects and even at low temperature resulting in a decrease in power output as a function of time.[6] All-oxide TE modules with direct oxide−oxide p−n junction would therefore be beneficial. However, such direct p−n junction will normally have high resistance because of charge carrier depletion in the space charge regions.[7]

Shin et al. demonstrated for the first time the prototype of a direct p−n oxide module using Li-doped NiO and (Ba, Sr)PbO$_3$, and 14 mW at $\Delta T = 552$ K was achieved.[8] Later, Hayashi et al. reported a stacked module with direct p−n oxide junctions based on p-type $(La_{1.97}Sr_{0.03})CuO_4$ and n-type $(Nd_{1.97}Ce_{0.03})CuO_4$, where the maximum power density obtained from 25 pairs was 40 mW/cm$^2$ at 400 °C and $\Delta T = 360$ K.[9] Moreover, Funahashi et al. demonstrated a module using a nonoxide p-type $Ni_{0.9}Mo_{0.1}$ and n-type $La_{0.035}Sr_{0.965}TiO_3$,[10] where the maximum obtained power density from 50 pairs was 450 mW/cm$^2$ at $\Delta T = 360$ K.

Furthermore, Chavez et al. showed another concept of using large-area p−n junctions (containing no insulator) as a TE module where 1.3 mW was generated from one pair at $\Delta T =$ 300 K.[11] The chemical compatibility, long-term stability, and electrical performance of the p−n junctions/modules were not considered in these studies.

$Ca_3Co_{4-x}O_{9+\delta}$ (CCO) has a misfit-layered complex crystal structure containing triangular $CoO_2$ and rock-salt $Ca_2CoO_3$ layers.[12] CCO shows p-type conductivity and exhibits excellent thermoelectric (TE) power at elevated temperatures in ambient air.[13] $CaMnO_{3-\delta}$ (CMO) has a perovskite structure and exhibits n-type conductivity resulting from an intrinsic oxygen deficiency. By introducing a secondary $CaMn_2O_4$ spinel phase, the TE properties of the $CaMnO_{3-\delta}$−$CaMn_2O_4$ composite are improved compared with single phase $CaMnO_{3-\delta}$, as observed in our research group. TE properties of these oxides can further be improved by doping or co-doping.[14] So far, only a few reports on conventional modules based on the CCO−CMO-based system are available.[15−22] Besides high-temperature TE modules, there are recently reported promising low-temperature organic-based TE modules, containing flexible layered design.[23,24]

Here, we report on high-temperature TE performance for an all-oxide TE module based on the system p-type $Ca_3Co_{4-x}O_{9+\delta}$ (CCO) and n-type $CaMnO_3$−$CaMn_2O_4$ (CMO-composite). $LaAlO_3$ (LAO) was selected as the electrical insulating component because of its ferroelastic properties[25] and high thermal expansion coefficient (TEC) compared with other potential insulating oxide candidates. Undoped CCO and a CMO-composite were selected as model materials in this work focusing on developing processing methods of the layered module and thereby analyzing the effect of a direct oxide−oxide p−n junction at high-temperature on TE performance of the module. The performance of the module critically depends on the properties of an in situ formed complex p−p−n junction, which was studied with respect to stability, interdiffusion, compatibility, and electrical conductivity. Finally, we report on an environment friendly processing method for all-oxide TE devices based on aqueous tape casting and co-sintering of the three materials using spark plasma sintering (SPS).

## 2. RESULTS

**2.1. Powder Characteristics.** X-ray diffraction (XRD) patterns of CCO, CMO-composite, and LAO powders are presented in Figure 1a, confirming the phase purity of CCO and LAO as well as the composite nature of the CMO-composite ($CaMnO_3$ with minor amount of $CaMn_2O_4$ secondary phase). XRD patterns of polycrystalline CCO prepared by SPS are also included in Figure 1a, both parallel and perpendicular to the pressing direction. A high degree of texture is observed (c oriented parallel to the pressing direction) as well as small amounts of $Ca_3Co_2O_6$ and $Co_3O_4$ secondary phases. Fine-grained powders of the three starting oxides are confirmed from the scanning electron microscopy (SEM) images in Figure 1b. Sintering curves for the CCO, CMO-composite, and LAO powders shown in Figure 1c demonstrate the onset of sintering at around 650, 900, and 1000 °C for CCO, CMO-composite, and LAO, respectively. TECs of CCO (perpendicular and parallel to pressing direction during SPS), CMO-composite, and LAO are summarized in Table 1. CCO and CMO-composite show similar TECs while LAO has a significantly lower value.
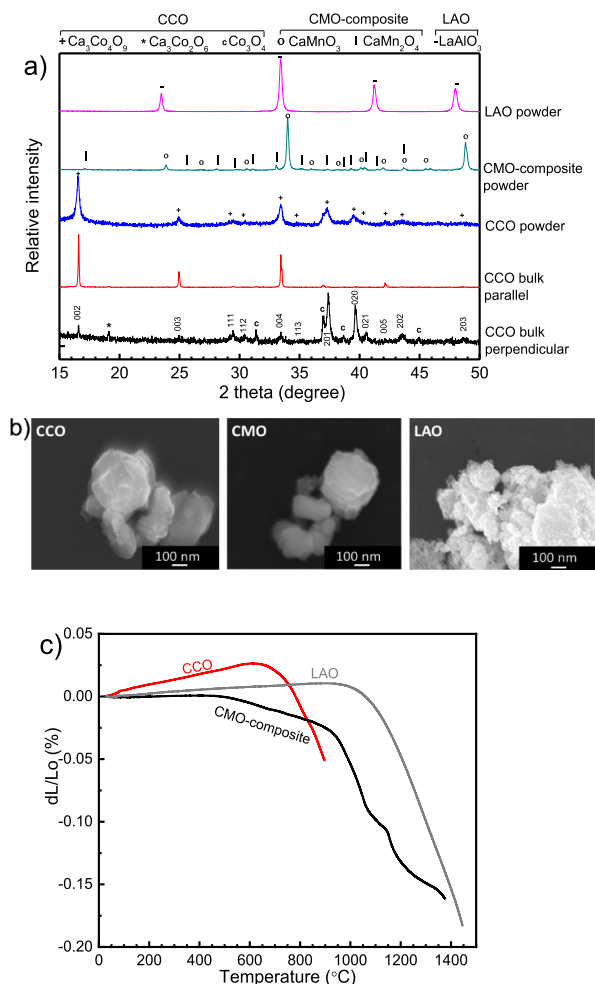


**Figure 1.** (a) XRD patterns of CCO, CMO-composite, and LAO powders as well as a sample of CCO made by SPS in the directions parallel and perpendicular to the pressing direction, (b) SEM micrographs, and (c) sintering curves of CCO, CMO-composite, and LAO powders produced by spray pyrolysis. Diffraction lines from articles, LAO,[25] CCO,[26] and CMO-composite powder ($CaMnO_3$[27] and $CaMn_2O_4$[28]) are indicated in (a).

**2.2. TE Performance of the Materials.** Electrical conductivity, thermal conductivity, Seebeck coefficient, power factor, and $zT$ as a function of temperature for the p- and n-type oxides are presented in Figure 2. CCO shows a maximum electrical conductivity in the range of 500−600 °C, reaching approximately 100 S cm$^{-1}$ (Figure 2a). On the other hand, the electrical conductivity of the CMO-composite has a constant value of 7 S cm$^{-1}$ up to 600 °C from where it increases to 28 S cm$^{-1}$ at 900 °C. The thermal conductivity of both materials decreases with temperature, reaching minima of 0.85 W m$^{-1}$ K$^{-1}$ at 700 °C for CCO and 1.42 W m$^{-1}$ K$^{-1}$ at 800 °C for the CMO-composite (Figure 2b). The sudden drop in thermal conductivity for CCO above 600 °C is most probably due to phonon−phonon interactions between the $a$−$b$ plane and $c$ direction due to the anisotropic crystal structure and texturing of the sample. A maximum Seebeck coefficient of 186 $\mu$V K$^{-1}$ at 500 °C for CCO and −325 $\mu$V K$^{-1}$ at 400 °C for the CMO-composite (Figure 2c) was achieved. A maximum power factor for CCO (3.6 $\mu$W cm$^{-1}$ K$^{-2}$) was obtained at ∼500 °C. The figure-of-merit, $zT$, presented in Figure 2d increased with temperature, reaching 0.39 at 700 °C for CCO and 0.05 at 800

**Table 1. TEC of CCO (Perpendicular and Parallel to the Pressing Direction During SPS), CMO, and LAO**

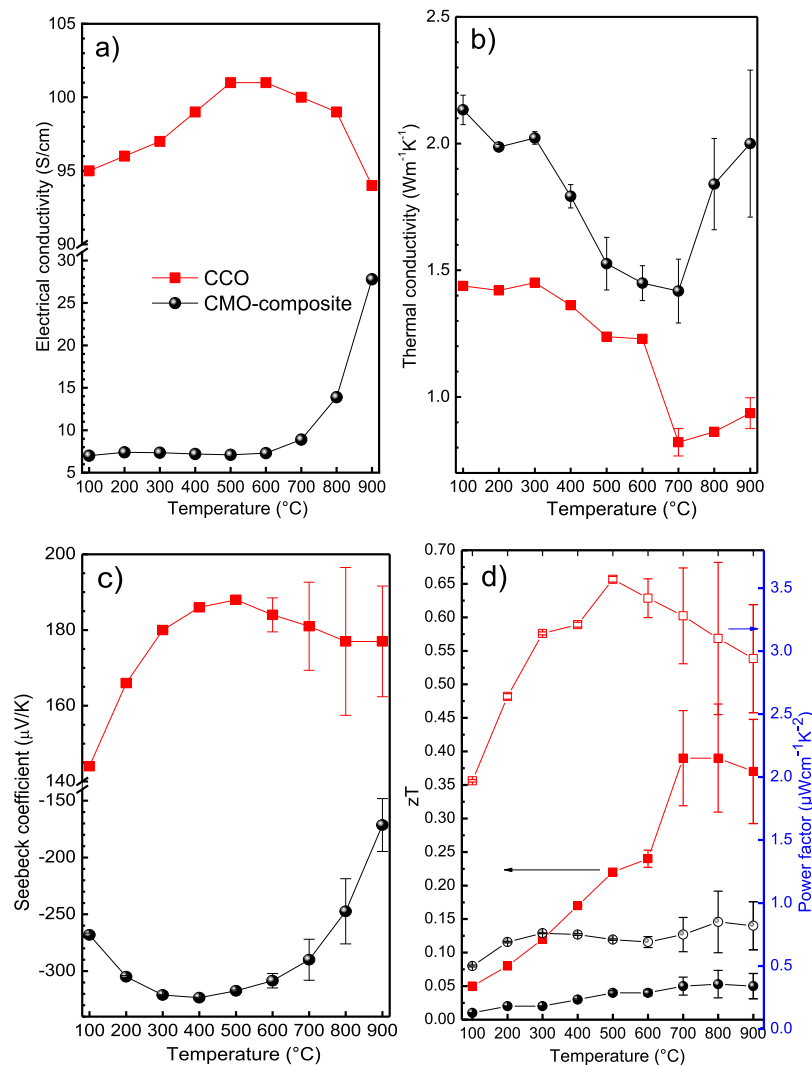| | CCO parallel to the pressing direction $(K^{-1} \cdot 10^{-6})$ | CCO perpendicular to the pressing direction $(K^{-1} \cdot 10^{-6})$ | LAO $(K^{-1} \cdot 10^{-6})$ | CMO-composite $(K^{-1} \cdot 10^{-6})$ |
|---|---|---|---|---|
| 400−800 °C (heating) | 17.0 | 14.4 | 9.7 | 18.0 |
| 700−400 °C (cooling) | 17.8 | 14.5 | 9.7 | 18.2 |



**Figure 2.** (a) Electrical conductivity, (b) thermal conductivity, (c) Seebeck coefficient, and (d) $zT$ (full symbols) and power factor (open symbols) as a function of temperature for CCO and CMO-composite ceramics. Error bars represent standard deviation based on five (Seebeck coefficient) and three (thermal conductivity) measured values. The uncertainty in electrical conductivity is smaller than the symbols and less than ±1%.

°C for the CMO-composite. The electrical conductivity and Seebeck coefficients were measured in the direction perpendicular to the pressing direction, whereas the thermal conductivity was recorded parallel to the pressing direction of the sample. The measurements in the two different orientations resulted in a higher $zT$ than the real one because the reported thermal conductivity of CCO is strongly anisotropic.[29]

**2.3. TE Module.** Schematic of the cross section of the TE module design is shown in Figure 3a. The thickness of the CMO-composite after co-sintering is approximately four times larger than the thickness of the CCO layer. Resistance, $R$, of both conductors was calculated by the formula $R = \rho \cdot l / A$ where $\rho$ is electrical resistivity (cm·S⁻¹), $l$ is height/length

(cm), and $A$ is area (cm²). The electrical resistance of CMO-composite at, for example, 800 °C is about 1.6 more than one of CCO, and therefore, the CMO-composite represents more electrically resistive part in spite of larger thickness compared with CCO and limits the charge carrier flow. Because of the significant increase in electrical conductivity of CMO-composite above 800 °C, and slight decrease of CCO, the electrical resistance of the CMO-composite at 900 °C is about 0.7 times less than one of CCO; hence, the CCO represents more electrically resistive part.

Voltage (polynomial fitting) and power output of the TE module as a function of measured current output are shown in Figure 3b. Dashed lines represent current and voltage at maximum power at 700, 800, and 900 °C at the hot side of the
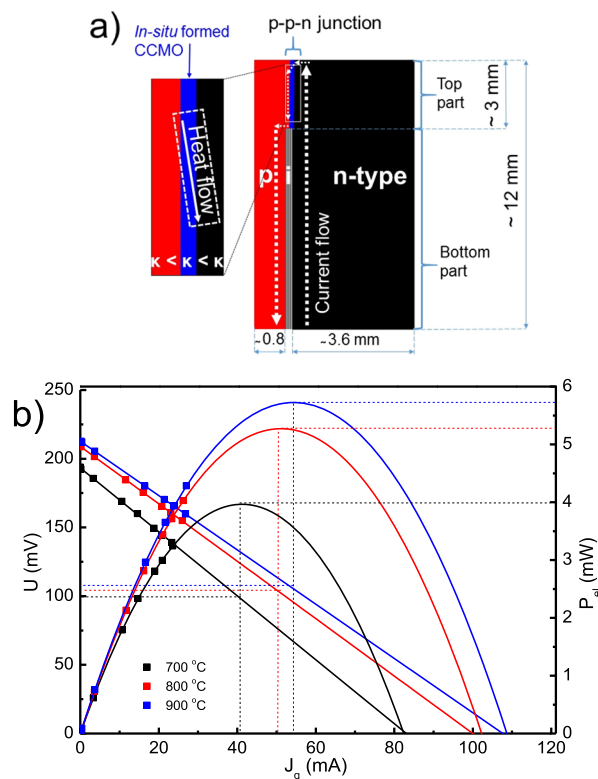
**Figure 3.** (a) Schematic of the cross section of the TE module with illustrated top part and bottom part (p- and n-type materials separated by an insulator, i) as well as flow direction of heat at top part (b) polynomial fitting of electrical power output ($P_{el}$) and linear fitting of voltage ($U$) as a function of the electrical current ($J_q$) at different $T_{hot}$ temperatures (700, 800, and 900 °C) and constant $\Delta T$ = 160 K. Voltage and current at maximum power $U(P_{max})$ and $J_q(P_{max})$ at different temperatures are also indicated by dotted lines.

module. Power output increases with temperature, reaching a maximum of about 5.7 mW at 900 °C. The effective power density of about 23 mW/cm$^2$ at this temperature was calculated from the effective area of TE module (approximately 0.25 cm$^2$).

Open-circuit voltage $U_{OC}$ and short-circuit current $J_{q,SC}$ were determined by extrapolation from the measured $J_q$−$U$ line and reached 213 mV and 108 mA at 900 °C, respectively. Data from the characterization of the TE module performance are summarized in Table 2.

Because the power output is dependent on load resistance, the maximum power output could be measured when the set-up-load from an external circuit of 5.7 Ω became equal to the TE module's resistance of about 2.1 Ω (at 800 °C).[30] The calculated figure of merit of the module ($ZT$) is 0.01, using

**Table 2. Open-Circuit Voltage $U_{OC}$, Short-Circuit Current $J_{q,sc}$, Electrical Resistance of the Module $R$, Electrical Power Output $P_{max}$, and Power Density of CCO−CMO TE Module at 700, 800, and 900 °C at 160 K Temperature Difference between the Hot and Cold Side**

| $T_h$ (°C) | $U_{oc}$ (mV) | $J_{q,sc}$ (mA) | $R_{module}$ (Ω) | $P_{max}$ (mW) | $P_{max}$ (mW/cm$^2$) |
|---|---|---|---|---|---|
| 700 | 181 | 82 | 2.2 | 4.0 | 16 |
| 800 | 208 | 101 | 2.1 | 5.2 | 21 |
| 900 | 213 | 108 | 2.0 | 5.7 | 23 |

$$ZT = \frac{U_{OC}}{J_{q,SC}R_{module}} - 1 \qquad (2)$$

where $U_{OC}$, $J_{q,SC}$, and $R_{module}$ represents open-circuit voltage, short-circuit current, and resistance of the module, respectively.[31]

**2.4. p−p−n Junction.** The microstructure of the CCO−CCMO−CMO p−p−n junction before and after annealing at 900 °C for 100 h is shown in Figure 4a. Elongated grain
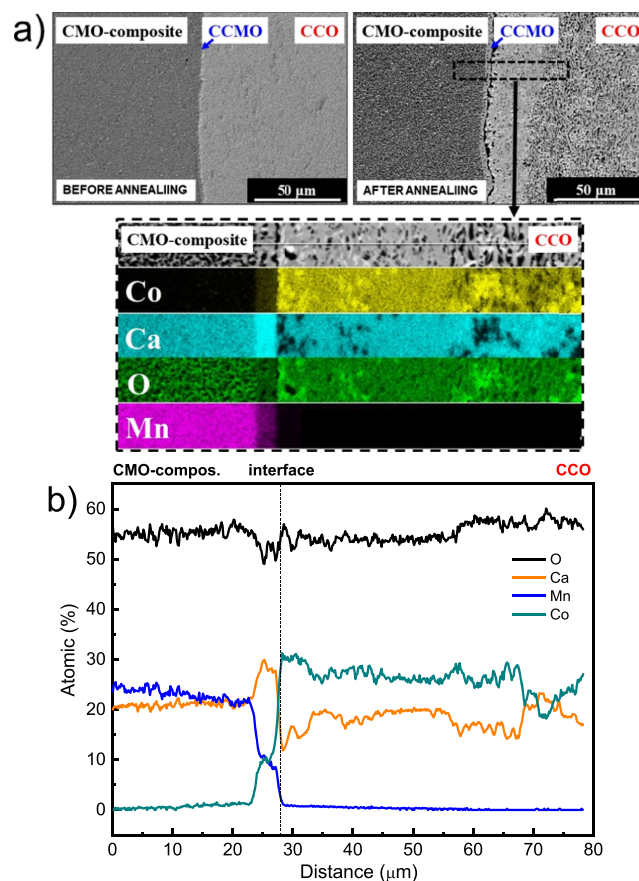


**Figure 4.** (a) SEM micrographs of CCO−CCMO−CMO junction before and after annealing at 900 °C for 100 h and EDS maps of the magnified section of the annealed junction given by the dashed lines and (b) EDS line profiles across the CCO−CCMO−CMO junction after annealing.

growth parallel to the interface is evident in CCO. A thin $Ca_3CoMnO_6$ (CCMO) layer, confirmed by energy-dispersive spectrometry (EDS), is formed in situ between CCO and CMO during the co-sintering. The CCMO layer has grown to approximately 5 μm after annealing at 900 °C for 100 h. In addition, a layer of approximately 35 μm thickness close to the interface displayed a higher density than the rest of the CCO. From the EDS profiles of the CCO−CMO interface presented in Figure 4b, the Ca content in this dense layer is lower than that in CCO showing a Co-rich and a Ca-deficient region at the interface. The Ca/Co ratio equals the initial Ca/Co ratio corresponding to pure CCO approximately 40 μm from the interface. A Co-oxide phase seen as grains with higher Co-content in Figure 4a is present both in the dense interface layer as well as in the CCO far from the interface.

Current−voltage curves across the CCO−CCMO−CMO complex junction before and after annealing at 900 °C for 100

h, measured at 300, 500, and 700 °C are presented in Figure 5a. Ohmic behavior is observed in the whole temperature
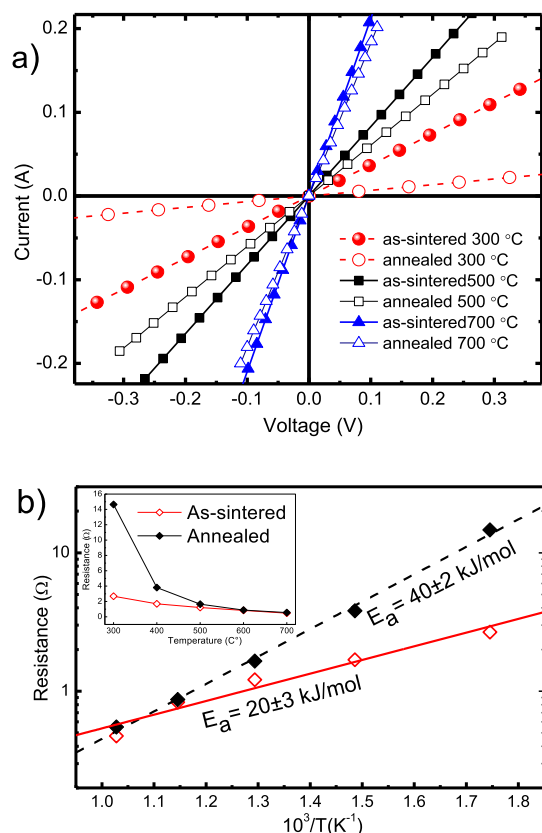


**Figure 5.** (a) Current−voltage curves of CCO−CMO−CMO p−p−n junctions before and after annealing at 900 °C for 100 h and (b). The activation energies for electrical conduction for the as-sintered and annealed sample. The inset shows resistance of p−p−n junctions before and after annealing as a function of temperature.

range for both as-sintered and annealed junctions, and the resistance decreases with increasing temperature. The difference in the resistance for the as-sintered and annealed samples is less pronounced as the temperature increases, and at 700 °C almost no difference is observed (inset in Figure 5b).

Figure 5 represents the activation energy for conduction of the as-sintered and annealed samples according to the Arrhenius equation, where the annealed sample demonstrates twice the activation energy of the as-sintered.

## 3. DISCUSSION

**3.1. Ceramic Processing.** A new co-sintering route to an all-oxide TE module was developed. The maximum sintering temperature was limited by the decomposition temperature of CCO. Moreover, CMO possesses a phase transition at 896−913 °C[32] from orthorhombic to tetragonal phase associated with a volume change, which also could introduce stresses in the device. Therefore, 880 °C was selected as the maximum co-sintering temperature. Because this temperature is low for efficient densification of CMO-composite and LAO (Figure 1c), a maximum pressure of 75 MPa was applied in the SPS with optimal 5 min hold, which resulted in 70 and 46% relative density for CMO-composite and LAO, respectively. CCO was completely densified after 2 min at 880 °C, but due to grain growth and micro-delamination, the final density after 5 min was 91% of theoretical. The CMO-composite possesses the highest TEC of the three materials (Table 1) and tensional stress is induced during cooling; hence, the CMO-composite represents the most sensitive part of the module during processing being prone to crack formation. The crack formation could be controlled by designing a thin CCO (~0.8 mm) and thick CMO (~3.6 mm) layer reducing the tensile stresses in the CMO-composite. The calculated tensile stresses in the CMO-composite (Supporting Information, Figure S2) developed during the cooling from 880 °C decreases both with increasing CMO-composite thickness and decreasing CCO thickness.[33]

**3.2. Origins of High Power Output and Open-Circuit Voltage.** As evident from Table 3, there are large differences in the output power of conventionally designed CCO−CMO TE modules dependent on whether CCO and CMO are doped or (like in our case) undoped, as well as on the applied temperatures and gradients.

Urata et al.[17] reported as much as 42.5 mW cm$^{-2}$ for a doped system with a $T_{hot}$ of about 900 °C and a gradient as high as 565 K, while undoped CCO−CMO systems at lower temperature and gradients of 200 K yielded merely 3.3 mW cm$^{-2}$ (Phaga et al.[16]) and 23.7 × 10$^{-3}$ mW cm$^{-2}$ (Seetawan et al.[15]).

Our prototype TE module with undoped CCO−CMO and a complex p−p−n junction could not be exposed to a larger $\Delta T$ than 160 K due to limitations of the set-up. Yet, a maximum power density of about 23 mW cm$^{-2}$ was generated at 900 °C. We attribute this to the remarkably high open-circuit voltage and low interface resistance of the complex p−p−n junction, as will be discussed next.

According to Kanas et al., electrical conductivity of the CCMO phase formed at the interface increases sharply with increasing temperature from 800 to 900 °C and reaches

**Table 3. TE Performance of Conventional Modules Based on p-Type CCO and n-Type CMO Reported in the Literature**

| system | N-pairs | $T_{hot}$ (K) | $\Delta T$ (K) | $P_{max}$ (mW) | $P_{density}$ (mW cm$^{-2}$) | P/one pair (mW) | references |
|---|---|---|---|---|---|---|---|
| $Ca_3Co_4O_9$, $CaMnO_3$ | 12 | 473 | 200 | 1.98 | 3.3[a] | 0.165[a] | Seetawan et al.[15] |
| $Ca_3Co_4O_9$, $CaMno_3$ | 31 | | 200 | 1.47 × 10$^{-3}$ | 23.7 × 10$^{-3a}$ | 4.74 × 10$^{-5a}$ | Phaga et al.[16] |
| $Ca_{2.7}Bi_{0.3}Co_4O_9$, $CaMn_{0.98}Mo_{0.02}O_3$ | 8 | 897 | 565 | 170 | 42.5 | 21.2[a] | Urata et al.[17] |
| $Ca_{2.75}Gd_{0.25}Co_4O_9$, $Ca_{0.92}La_{0.08}MnO_3$ | 8 | 773 | 390 | 63.5 | 44.1 | 7.9[a] | Matsubara et al.[18] |
| $Ca_3Co_4O_9$, $Ca_{0.95}Sm_{0.05}MnO_3$ | 2 | 1000 | 925 | 31.5 | 49.2[a] | 15.7[a] | Reddy et al.[19] |
| $Ca_3Co_4O_9$, $Ca_{0.9}Nd_{0.1}MnO_3$ | 1 | 1175 | 727 | 95 | 93.2 | 95 | Lim et al.[20] |
| $Ca_{0.76}Cu_{0.24}Co_4O_9$, $Ca_{0.8}Dy_{0.2}MnO_3$ | 4 | | 346 | 8.42 | | 2.1[a] | Park et al.[21] |
| $Ca_3Co_4O_9$, $Ca_{0.95}Sm_{0.05}MnO_3$ | 2 | 990 | 630 | 31.5 | 49.2 | 15.7[a] | Noudem et al.[22] |

[a]The values marked with are calculated, based on the data available in the given references.

around 0.1 S cm$^{-1}$ at 900 °C, where the positive Seebeck coefficient furthermore reaches as high as 668 $\mu$V K$^{-1}$.[34] The three-layered CCO−CCMO−CMO junction exhibits Ohmic behavior with relatively modest interfacial resistance above 700 °C as evidenced in Figure 5a. We tentatively interpret this as an effect of the electron energy levels of CCMO as laying intermediate of those of CCO and CMO, hence decreasing the depletion of charge carriers at the CCO−CCMO and CCMO−CMO interfaces as compared to a hypothetical pristine CCO−CMO p−n interface. This facilitates an electrical current flow through the p−p−n interface as illustrated in Figure 3a.

The CCMO reaction layer is thicker in the annealed sample compared with the as-sintered one (Figure 4a), and in the temperature range 300−500 °C, resistivity is higher for the annealed sample (Figure 5). At 700 °C, the resistivity of both samples are almost equal (Figure 5), showing that the same concentration of charges will be excited to conduction level because of thermal activation, demonstrating no effect of CCMO thickness on the current density above 700 °C. The CCMO layer is therefore contributing equally to the electrical conduction process at this high temperature.

When two materials A and B dissimilar in thermal conductivity and Seebeck coefficient are contacted over an area exposed to a parallel thermal gradient, a voltage is generated in the transversal direction, and an effective transversal Seebeck coefficient of the couple can be expressed according to Goldsmid[35]

$$S_{yo} = (S_A/K_A + S_B/K_B)/(1/K_A + 1/K_B) \qquad (3)$$

where $S_A$, $S_B$, $K_A$, and $K_B$ represent the Seebeck coefficients and thermal resistances of the two materials. In our case, the thermal conductivity of CCO at 900 °C is 0.94 W m$^{-1}$ K$^{-1}$ while that for CCMO is 1.3 W m$^{-1}$ K$^{-1}$[34] and the CMO-composite is 2.0 W m$^{-1}$ K$^{-1}$. This will give rise to different heat flows down the n- and p-type materials, resulting in an increasing transversal temperature gradient down the CCMO interface layer corresponding to the transversal heat flow illustrated in Figure 3a.

For the following discussion, the module may be divided into a top hot part above the LAO insulator and a bottom conventional part. The top part contains three material layers and two subjunctions which contribute to a transversal TE voltage according to eq 3, whereas the bottom part contributes to standard longitudinal TE voltages. On the basis of the dimensions of the module, we may estimate a temperature difference of 40 K over the top part and the remaining 120 K cover the bottom part. Because the Seebeck coefficient of CMO is strongly influenced by temperature (Figure 2c), average values are used for summing up all possible contributions from materials and interfaces in the transversal and longitudinal parts. We arrive at an estimated open-circuit potential of 125 mV, as compared to the estimate of 64 mV from a regular CCO and CMO couple with a total gradient of 160 K, based on their Seebeck coefficients of +177 and −171 $\mu$V K$^{-1}$ (at 900 °C) and about +179 and −270 $\mu$V K$^{-1}$ (at approximately 740 °C), respectively. Average absolute values of the Seebeck coefficient and thermal conductivity of CCO and CMO for the top and bottom parts of the module used for the calculations are 178 $\mu$V K$^{-1}$ (CCO$_{bottom}$), 177 $\mu$V K$^{-1}$ (CCO$_{top}$), 0.89 W m$^{-1}$ K$^{-1}$ (CCO$_{top}$), 229 $\mu$V K$^{-1}$ (CMO$_{bottom}$), 189 $\mu$V K$^{-1}$ (CMO$_{top}$), and 1.88 W m$^{-1}$ K$^{-1}$ (CMO$_{top}$). A transversal TE effect occurs when anisotropy in

the electrical and thermal transport occurs,[35] as in our top part of the module. This phenomenon is beneficially used for enhancing the voltage in transversal TE modules and related applications.[36−40] For instance, the transversal TE voltage in Ca$_x$CoO$_2$ textured thin films can be significantly higher than the ones generated by regular TE effect.[36−38] The transversal voltage significantly affected the open-circuit voltage $U_{OC}$ and the maximum electrical power output $P_{el}$. The presence of a transverse TE effect can also be observed by comparison of $U_{OC}$ of the TE module (Figure 3b) and Seebeck coefficient together with the power factor of individual materials from 700 to 900 °C. The Seebeck coefficients (Figure 2c) of the two individual materials decrease as temperature increases, as well as power factor of CCO (Figure 2d), whereas $U_{OC}$ of TE module increases with temperature (Figure 3b). The experimentally measured $U_{OC}$ of 213 mV is hence remarkably larger than both theoretical estimates. Further experimental and theoretical studies (e.g., field emission microscopy simulations) will be necessary to fully understand the effect of thin layers of materials with high Seebeck coefficients in the interface of p−n TE junctions. However, the in situ formed complex p−p−n junctions evidently improved the performance of the all-oxide TE module, hence representing a significant step forward toward the possible application of oxide TE modules in high-temperature energy recovery.

## 4. CONCLUSIONS

A novel all-oxide TE module was successfully developed and fabricated by careful processing of materials in the CCO−CMO system using LAO as an electrical insulator. Fabrication of this all-oxide TE module is simpler and faster than assembling conventional modules. The CCO−CMO module demonstrated a power of about 5.7 mW corresponding to a power density of 23 mW cm$^{-2}$ at $T_{hot}$ = 900 °C and $\Delta T$ = 160 K, a TE performance comparable and better than some conventional CCO−CMO modules. The all-oxide layered TE module produces a large open-circuit voltage, which was attributed to the presence of a thin CCMO reaction layer and transversal TE effect across the top p−p−n part of the TE module. The effect of the CCMO reaction layer is due to the large Seebeck coefficient, working transversally and reducing the charge carrier depletion and resistance at the high-temperature p−n junction. The present investigation demonstrates an example of novel engineering of oxide TE modules without metallic interconnects.

## 5. EXPERIMENTAL SECTION

**5.1. Materials and Ceramic Processing.** The ceramic powders used in this work were prepared by spray pyrolysis (CerPoTech AS, Norway). Slurry for aqueous tape casting of the LAO insulator was prepared according to the schematics shown in Figure S1 (Supporting Information). The slurry was casted on a polyester (Mylar) film using a height of the doctor blade of 30 $\mu$m. After drying at ambient temperature, lamination of 8 layers was conducted by hot-pressing at 150 MPa and 80 °C for 3 min. The laminated tape was cut into 12 mm discs with one segment cut off (around 3 mm) to make the direct p−n junction. Binder burnout was done at 440 °C for 4 h in air, placing the tape between two alumina plates to avoid bending. The TE module was fabricated by SPS (Dr. Sinter 825) in a 12 mm graphite die at 880 °C and 75 MPa for 5 min using heating and cooling rates of 120 °C/min. Initially,

the graphite die was filled with the CMO-composite powder (1.5 g), and then the cut LAO tape was placed on CMO-composite powder, followed by filling of CCO powder (0.5 g) onto the LAO tape.

In addition, CMO-composite and CCO materials were separately sintered by SPS using the same conditions as used for the TE module. These pellets were cut into a bar-shape (20 × 5 × 2.5 mm) for electrical conductivity and Seebeck coefficient measurements and discs (12.7 mm diameter) for thermal conductivity measurements. Densities of pellets and bars were determined by Archimedes measurement in isopropanol. To do a separate analysis of the direct CCO−CMO-composite junction, two samples were prepared by SPS co-sintering at 820 °C and 50 MPa for 10 min. One of these samples was further annealed at 900 °C for 100 h in air.

**5.2. Characterization.** Phase composition and particle size/morphology were characterized by powder X-ray diffraction (Bruker D8 DAVINCI) and SEM (Hitachi S-3400N), respectively. Sinterability and TEC were determined by dilatometer (Netzsch DIL 402) in ambient air. TEC was measured both parallel and perpendicular to the pressing direction for CCO made by SPS. TE performance of CCO and CMO materials were analyzed by measuring Seebeck coefficient (ProboStat, NorECs AS), electrical conductivity (home-made setup) and thermal conductivity (Netzsch LFA 457 MicroFlash) at 100−900 °C in ambient air as described elsewhere.[41,42]

For the power−current−voltage characterization, the layered disc-shaped TE module was placed horizontally on an alumina plate with the direct p−n junction at the top (hot temperature side).

To ensure better physical stability of the free-standing module, a small area of about 0.25 cm² was removed on the cold side. Both semiconductors were contacted by Pt-wires at the lower, colder end, using gold paste (Heraeus). The alumina plate with the TE module connected to Pt-wires was heated at 700 °C for 4 h in ambient air, to establish good electrical contact between the metal electrodes and semiconducting oxides.

The power output test in ambient air was performed via load resistance-dependent measurement, in a vertical furnace at 700, 800, and 900 °C, and $\Delta T$ = 160 K. The temperature gradient was established by heating the hot side of the module in the furnace, whereas the cold side was cooled by an active cooler. The temperature difference $\Delta T$ was measured by two Pt−Pt10Rh (type S) thermocouples. During the power output measurement, the voltmeter was connected parallel to the amperemeter, variable resistor (in series to each other), and to the TE module. When thermal equilibria were established at each temperature, electrical current and voltage were measured with increasing load resistance. More details could be found in ref 4.

Finally, annealed and as-sintered p−n junctions were characterized by current−voltage measurements at 300, 500, and 700 °C in a vertical furnace, using a ProboStat cell (NORECS, Norway). A two-electrode set-up was used, where a dc voltage was applied to the junction followed by measuring current output using Multimeter-Agilent E3642A. After the measurements, the samples were embedded in "EpoFix" resin, polished by diamond paste (DiaPro NapB1) to 1 $\mu$m and coated with carbon (Cressington Carbon Coater 208) for microstructural characterization. Interface reaction and inter-

diffusion at the p−n junction were investigated using SEM and EDS (Hitachi S-3400N).

## ■ ASSOCIATED CONTENT

**ⓢ Supporting Information**

The Supporting Information is available free of charge on the ACS Publications website at DOI: 10.1021/acsomega.8b01357.

Material supplied as Supporting Information contains further experimental details and estimated tensile stresses developed in CMO in the co-sintered module (PDF)

## ■ AUTHOR INFORMATION

**Corresponding Author**
*E-mail: mari-ann.einarsrud@ntnu.no (M.-A.E.).

**ORCID** ⓞ
Temesgen Debelo Desissa: 0000-0003-3612-7153
Mari-Ann Einarsrud: 0000-0002-3017-1156

**Notes**
The authors declare no competing financial interest.

## ■ REFERENCES

(1) Walia, S.; Balendhran, S.; Nili, H.; Zhuiykov, S.; Rosengarten, G.; Wang, Q. H.; Bhaskaran, M.; Sriram, S.; Strano, M. S.; Kalantar-zadeh, K. Transition metal oxides—Thermoelectric properties. *Prog. Mater. Sci.* **2013**, 58, 1443−1489.

(2) Sootsman, J. R.; Chung, D. Y.; Kanatzidis, M. G. New and Old Concepts in Thermoelectric Materials. *Angew. Chem. Int. Ed.* **2009**, 48, 8616−8639.

(3) Ioffe, A. F. *Semiconductor Thermoelements and Thermoelectric cooling*, 1st ed.; Info-search Ltd.: London, 1957.

(4) Bittner, M.; Geppert, B.; Kanas, N.; Singh, S. P.; Wiik, K.; Feldhoff, A. Oxide-based thermoelectric generator for high-temperature application using p-type $Ca_3Co_4O_9$ and n-type $In_{1.95}Sn_{0.05}O_3$ legs. *Energy Harvest. Syst.* **2016**, 3, 213−222.

(5) Tomeš, P.; Robert, R.; Trottmann, M.; Bocher, L.; Aguirre, M. N.; Bitschi, A.; Hejtmánek, J.; Weidenkaff, A. Synthesis and characterization of new ceramic thermoelectrics implemented in a thermoelectric oxide module. *J. Electron. Mater.* **2010**, 39, 1696−1703.

(6) Barako, M. T.; Park, W.; Marconnet, A. M.; Asheghi, M.; Goodson, K. E. Thermal cycling, mechanical degradation, and the effective figure of merit of a thermoelectric module. *J. Electron. Mater.* **2013**, 42, 372−381.

(7) Streetman, B. G.; Banerjee, S. K. *Solid State Electronic Devices*, 6th ed.; PHI Learning Private Limited: New Delhi, 2009.

(8) Shin, W.; Murayama, N.; Ikeda, K.; Sago, S. Thermoelectric power generation using Li-doped NiO and (Ba, Sr)PbO3 module. *J. Power Sources* **2001**, 103, 80−85.

(9) Hayashi, S. F.; Nakamura, T.; Kageyama, K.; Takagi, H. Monolithic thermoelectric devices prepared with multilayer cofired ceramics technology. *Jpn. J. Appl. Phys.* **2010**, 49, 096505.

(10) Funahashi, S.; Nakamura, T.; Kageyama, K.; Ieki, H. Monolithic oxide-metal composite thermoelectric generators for energy harvesting. *J. Appl. Phys.* **2011**, *109*, 124509.

(11) Chavez, R.; Angst, S.; Hall, J.; Stoetzel, J.; Kessler, V.; Bitzer, L.; Maculewicz, F.; Benson, N.; Wiggers, H.; Wolf, D.; Schierning, G.; Schmechel, R. High Temperature Thermoelectric Device Concept Using Large Area PN Junctions. *J. Electron. Mater.* **2014**, *43*, 2376−2383.

(12) Masset, A. C.; Michel, C.; Maignan, A.; Hervieu, M.; Toulemonde, O.; Studer, F.; Raveau, B.; Hejtmanek, J. Misfit-layered cobaltite with an anisotropic giant magnetoresistance:Ca3Co4O9. *Phys. Rev. B: Condens. Matter Mater. Phys.* **2000**, *62*, 166−175.

(13) Takeuchi, T.; Kondo, T.; Soda, K.; Mizutani, U.; Funahashi, R.; Shikano, M.; Tsuda, S.; Yokoya, T.; Shin, S.; Muro, T. Electronic structure and large thermoelectric power in Ca3Co4O9. *J. Electron Spectrosc.* **2004**, *137-140*, 595−599.

(14) Fergus, J. W. Oxide materials for high temperature thermoelectric energy conversion. *J. Eur. Ceram. Soc.* **2012**, *32*, 525−540.

(15) Seetawan, T.; Singsoog, K.; Srichai, S.; Thanachayanont, C.; Amornkitbamrung, V.; Chindaprasirt, P. Thermoelectric Energy Conversion of p-Ca3Co4O9/n-CaMnO3 Module. *Energy Proc.* **2014**, *61*, 1067−1070.

(16) Phaga, P.; Vora-Ud, A.; Seetawan, T. Invention of low cost thermoelectric generators. *Procedia Eng.* **2012**, *32*, 1050−1053.

(17) Urata, S.; Funahashi, R.; Mihara, T. *Proceedings of the International Conference on Thermoelectrics 2006, Vienna, Austria*, (6-10 Aug 2006), p 501.

(18) Matsubara, I.; Funahashi, R.; Takeuchi, T.; Sodeoka, S.; Shimizu, T.; Ueno, K. Fabrication of an all-oxide thermoelectric power generator. *Appl. Phys. Lett.* **2001**, *78*, 3627−3629.

(19) Reddy, E. S.; Noudem, J. G.; Hebert, S.; Goupil, C. Fabrication and properties of four-leg oxide thermoelectric modules. *J. Phys. D: Appl. Phys.* **2005**, *38*, 3751−3755.

(20) Lim, C.-H.; Choi, S.-M.; Seo, W.-S.; Park, H.-H. A Power-Generation Test for Oxide-Based Thermoelectric Modules Using p-Type Ca3Co4O9 and n-Type Ca0.9Nd0.1MnO3 Legs. *J. Electron. Mater.* **2012**, *41*, 1247−1255.

(21) Park, K.; Lee, G. W. Fabrication and thermoelectric power of π-shaped Ca3Co4O9/CaMnO3 modules for renewable energy conversion. *Energy* **2013**, *60*, 87−93.

(22) Noudem, J. G.; Lemonnier, S.; Prevel, M.; Reddy, E. S.; Guilmeau, E.; Goupil, C. Thermoelectric ceramic for generators. *J. Eur. Ceram. Soc.* **2008**, *28*, 41−48.

(23) Wu, G.; Gao, C.; Chen, G.; Wang, X.; Wang, H. High-performance organic thermoelectric modules based on flexible films of a novel n-type single-walled carbon nanotube. *J. Mater. Chem. A* **2016**, *4*, 14187−14193.

(24) Wu, G.; Zhang, Z.-G.; Li, Y.; Gao, C.; Wang, X.; Chen, G. Exploring high-performance n-type thermoelectric composites using amino-substituted rylene dimides and carbon nanotubes. *ACS Nano* **2017**, *11*, 5746−5752.

(25) Islam, M. N.; Araki, W.; Arai, Y. Mechanical behavior of ferroelastic LaAlO 3. *J. Eur. Ceram. Soc.* **2017**, *37*, 1665−1671.

(26) Kang, M.-G.; Cho, K.-H.; Kim, J.-S.; Nahm, S.; Yoon, S.-J.; Kang, C.-Y. Post-calcination, a novel method to synthesize cobalt oxide-based thermoelectric materials. *Acta Mater.* **2014**, *73*, 251−258.

(27) Wang, Y. X.; Du, Y.; Qin, R. W.; Han, B.; Du, J.; Lin, J. H. Phase equilibrium of the La-Ca-Mn-O system. *J. Solid State Chem.* **2001**, *156*, 237−241.

(28) Zouari, S.; Ranno, L.; Cheikh-Rouhou, A.; Isnard, O.; Pernet, M.; Wolfers, P.; Strobel, P. New model for the magnetic structure of the marokite-type oxide CaMn2O4. *J. Alloys Compd.* **2003**, *353*, 5−11.

(29) Bittner, M.; Helmich, L.; Nietschke, F.; Geppert, B.; Oeckler, O.; Feldhoff, A. Porous Ca 3 Co 4 O 9 with enhanced thermoelectric properties derived from Sol-Gel synthesis. *J. Eur. Ceram. Soc.* **2017**, *37*, 3909−3915.

(30) Priya, S.; Inman, D. J. *Energy Harvesting Technologies*; Springer: New York, 2009.

(31) Rowe, D. M.; Snyder, J. G. *Thermoelectrics Handbook: Macro to Nano*, 1st ed.; CRC Taylor and Francis: Boca Raton, 2006; p. 9.

(32) Taguchi, H.; Nagao, M.; Sato, T.; Shimada, M. High-temperature phase transition of CaMnO3−δ. *J. Solid State Chem.* **1989**, *78*, 312−315.

(33) Faaland, S. Heterogeneous ceramic interfaces in solid oxide fuel cells and dense oxygen permeable membranes. PhD Thesis, Norwegian University of Science and Technology NTNU: Trondheim, Norway, 2000.

(34) Kanas, N.; Singh, S. P.; Desissa, T. D.; Norby, T.; Wiik, K.; Grande, T.; Einarsrud, M.-A. Thermoelectric properties of Ca3Co2-xMnxO6, x = 0.05, 0.2, 0.5, 0.75 and 1. To be submitted.

(35) Goldsmid, H. J. Application of the transverse thermoelectric effects. *J. Electron. Mater.* **2011**, *40*, 1254−1259.

(36) Teichert, S.; Bochmann, A.; Reimann, T.; Schulz, T.; Dreßler, C.; Töpfer, J. An oxide-based thermoelectric generator: Transversal thermoelectric strip-device. *AIP Adv.* **2015**, *5*, 077105-1-6. DOI: 10.1063/1.4926384

(37) Kanno, T.; Takahashi, K.; Sakai, A.; Tamaki, H.; Kusada, H.; Yamada, Y. Detection of Thermal Radiation, Sensing of Heat Flux, and Recovery of Waste Heat by the Transverse Thermoelectric Effect. *J. Electron. Mater.* **2014**, *43*, 2072−2080.

(38) Takahashi, K.; Kanno, T.; Sakai, A.; Tamaki, H.; Kusada, H.; Yamada, Y. Bifunctional thermoelectric tube made of tilted multilayer material as an alternative to standard heat exchangers. *Sci. Rep.* **2013**, *3*, 1501.

(39) Takahashi, K.; Kanno, T.; Sakai, A.; Adachi, H.; Yamada, Y. Light-induced off-diagonal thermoelectric effect via indirect optical heating of incline-oriented CaxCoO2 thin film. *Appl. Phys. Lett.* **2012**, *100*, 181907.

(40) Yan, G.; Wang, S.; Chen, S.; Liu, F.; Bai, Z.; Wang, J.; Yu, W.; Fu, G. The effect of microstructure on the laser-induced transverse voltage in Pb-doped Bi2Sr2Co2O y thin films on tilted substrates. *Appl. Phys. A* **2013**, *111*, 1203−1206.

(41) Øygarden, V.; Grande, T. Crystal structure, electrical conductivity and thermal expansion of Ni and Nb co-doped LaCoO3. *Dalton Trans.* **2013**, *42*, 2704−2715.

(42) Wærnhus, I.; Vullum, P. E.; Holmestad, R.; Grande, T.; Wiik, K. Electronic properties of polycrystalline LaFeO₃. Part 1: Experimental results and the quantitative role of Schottky defects. *Solid State Ionics* **2005**, *176*, 2783−2790.